Engineering Fracture Mechanics 269 (2022) 108558

Contents lists available at ScienceDirect

Engineering Fracture Mechanics

journal homepage: www.elsevier.com/locate/engfracmech

On the failure assessment diagram methodology in polyamide 12

M. Martínez, A.J. Cano, A. Salazar, J. Rodríguez *

Grupo de Durabilidad e Integridad Mecánica de Materiales Estructurales (DIMME), Escuela Superior de Ciencias Experimentales y Tecnología, Universidad Rey Juan Carlos. C/ Tulipán, s/n, 28933 Móstoles, España

ARTICLE INFO

Keywords:
Failure Assessment Diagrams
Thermoplastics
Structural Integrity
Additive Manufacturing
Polyamide

ABSTRACT

For the first time, the Failure Assessment Diagrams of Polyamide 12, PA12, processed via a conventional technique as injection moulding, IM, and an additive manufacturing technique as Selective Laser Sintering, SLS, were determined via Finite Element Analysis (FEA) using a stress–strain equation more appropriate to describe the mechanical behaviour of thermoplastics. These diagrams were compared with those computed from the options of the BS 7910 standard applied for metals. The diagrams of SLS PA12 were clearly above that of IM PA12, presenting almost constant fracture ratio values for all the load ratios. This indicates the brittle behaviour, with small deviation from linearity, of SLS PA12 in comparison with IM PA12 which exhibited plasticity effects. This trend was supported by the mechanical response shown by PA12 manufactured by the different processing techniques. On the other hand, the diagrams obtained via FEA showed significant differences with the options of the BS 7910 standard, employed for the determination of the failure diagrams in metals, particularly when a Ramberg-Osgood model is used to describe the mechanical behaviour.

1. Introduction

The proliferation of new materials for structural use is evident in a wide variety of fields, especially in the transport sector. Among them, polymers and composites made of polymeric matrix are gaining more and more ground over metals, because the former can reduce the structural weight of a transport vehicle with the consequent reduce in fuel consumption. The substitution of the traditional engineering materials by polymers is accelerating thanks to the increasingly establishment of the Additive Manufacturing (AM) techniques. These techniques allow the manufacture of customized pieces without geometric limitation and without the need for tools in very short times. Of all the AM techniques, Selective Laser Sintering (SLS) stands out because it allows the manufacture of parts from a wide family of materials including polymers, metals, and various types of composite materials. Within the field of polymeric materials, polyamide 12 (PA12) prevails as it is ideal for this technique due to the large separation between melting and crystallization temperatures, low melt viscosity and high surface tension [1–6]. In addition, it is a light thermoplastic with good impact resistance, excellent mechanical properties and high resistance to fatigue, coupled with a low cost. This makes it a very attractive material for aeronautical and aerospace transport, for automobile construction, in biomedical engineering, in electrical applications and in the sports sector.

Failure Assessment Diagrams (FAD) are a tool for structural design against fracture combined with plasticity to assess the integrity of components containing flaws. The FAD approach is very versatile as it addresses elastoplastic problems in terms of two parameters

* Corresponding author.
E-mail address: jesus.rodriguez.perez@urjc.es (J. Rodríguez).

https://doi.org/10.1016/j.engfracmech.2022.108558
Received 15 February 2022; Received in revised form 29 April 2022; Accepted 17 May 2022
Available online 21 May 2022
0013-7944/© 2022 The Authors. Published by Elsevier Ltd. This is an open access article under the CC BY-NC-ND license (http://creativecommons.org/licenses/by-nc-nd/4.0/).

Nomenclature

a	Crack length
B	Specimen's thickness
E	Elastic modulus
$f(a/W)$	Geometric dependent factor for the determination K_I
h	G'Sell et al.'s hardening law constant
J	J-integral
J_{Ic}	Critical value of J-integral for mode I
K	G'Sell et al.'s hardening law constant
K^*	Simplified G'Sell et al.'s hardening law constant
K_I	Mode I stress intensity factor
K_{mat}	Fracture toughness
K_r	Fracture ratio
L_r	Load ratio
m	G'Sell et al.'s hardening law constant
N	BS 7910 option 1 constant
P	Applied load
P_L	Plastic collapse load
P_{prop}	Applied load at the crack propagation
S	Span between supports in three-point-bending tests
W	Specimen's width
ε	Strain
ε_{ref}	Reference strain
ε_v	G'Sell et al.'s hardening law constant
$\dot{\varepsilon}$	Strain rate
μ	BS 7910 option 1 constant
σ	Stress
σ_U	Tensile strength
σ_y	Yield strength

that vary linearly with the applied load. One of the parameters is the fracture ratio, K_r, defined as:

$$K_r = \frac{K_I}{K_{mat}} \tag{1}$$

where K_I is the applied mode I stress intensity factor and the K_{mat} is the fracture toughness of the material. The other is the load ratio, L_r, given by:

$$L_r = \frac{P}{P_L} \tag{2}$$

with P the applied load and P_L the plastic collapse load. The failure or limiting conditions of a structural component are represented in a $K_r - L_r$ diagram. This curve delimits the regions of failure and integrity of the component from the cases of brittle fracture to those of plastic collapse [7].

The development of FADs is linked to metallic components, with two standards of special relevance BS 7910 [8] and API 579 [9]. The problem of applying the FAD methodology to structural components made of polymers is that the BS 7910 [8] and API 579 [9] standards do not take into account the peculiarities that materials other than metallic may present. Polymers are viscoelastic and most of the thermoplastic materials present a stress–strain data that cannot be described by the Ramberg-Osgood model, commonly associated with metals. The typical engineering stress–strain curve obtained from a uniaxial tensile test of a thermoplastic material is characterised by an abrupt drop after yielding, commonly associated with the initial neck formation, followed by a plateau due to the stabilization and propagation of the neck along the gage length up to a hardening region prior to final rupture [10–13]. The true stress–strain curve of thermoplastics is characterised by an increasing rate of strain hardening, which cannot be described with a Ramberg-Osgood model. G'Sell et al. [10–12] proposed a hardening law to account for this characteristic behaviour of thermoplastic polymers, given by [12].

$$\sigma = K\left(1 - e^{-\varepsilon/\varepsilon_v}\right)e^{h\varepsilon^2}\dot{\varepsilon}^m \tag{3}$$

Where K is a material constant related to the yield strength, ε_v is a constant associated with the strain at the yield point, h considers the material strain hardening and m a constant. In its general form, the hardening law is strain rate, $\dot{\varepsilon}$, dependent.

The literature concerning the application of the FAD approach to polymeric structural components is very scarce. Cicero et al. [14–16] applied the methodology of the FAD in combination with the theory of the critical distances to determine the integrity of

Table 1
Manufacturing parameters of IM PA12.

Mould temperature	Filling time	Holding time	Injection speed	Injection pressure	Mould clamping force
60 °C	2.1 s	6.5 s	6–8 mm/s	10 MPa	1500 N

Table 2
Manufacturing parameters of SLS PA12.

Particle diameter	Powder bed temperature	Frame temperature	Layer thickness	Laser power
40–90 μm	171.5 °C	135.5 °C	0.2 mm	25 W

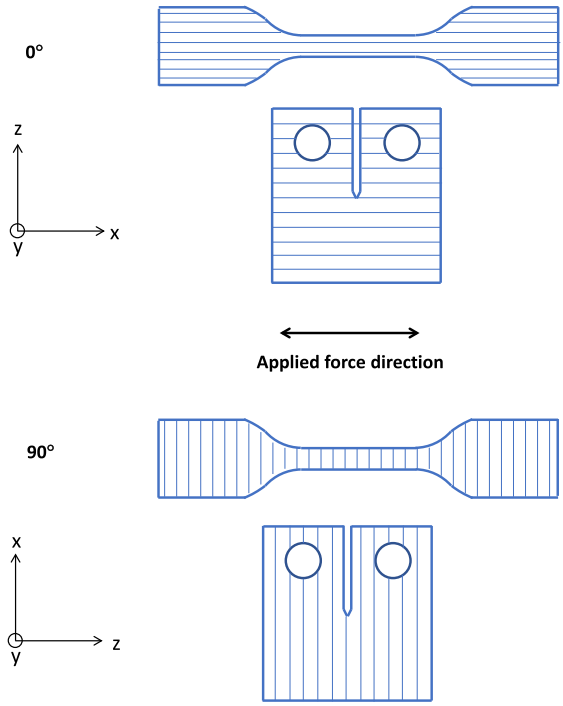

Fig. 1. Dumbbell shape and compact tension specimens fabricated by SLS where lines display layer orientation (z-axis perpendicular to the material layers).

notched samples made of non-metals, specifically of PMMA and of short fibre reinforced polyamide 6. Nevertheless, they did not take into account the peculiarities of these materials as they applied the recommendations of BS 7910 without modification.

The objective of this work is the application of the failure diagram methodology to PA12, assuming that its hardening behaviour can be described by G'Sell et al. equation [10–12]. The locus of failure will be determined by means of numerical simulation and the diagrams so obtained will be compared with those corresponding to the options offered by the BS 7910 standard. Three batches of PA12 were investigated. One of them was manufactured by the conventional technique as injection moulding, while the other two by the additive manufacturing technique as Selective Laser Sintering. As this layer-by-layer processing technique can induce anisotropy in the final microstructure, the mechanical characterization was performed in two batches. In one of them the layered structure was parallel and in the other perpendicular to the applied load. Therefore, the influence on the failure diagrams of the manufacturing technique and of the orientation of the layers in the SLS specimens was investigated.

2. Experimental procedure

2.1. Materials

The polyamide 12 under study was manufactured via injection moulding (IM) and Selective Laser Sintering (SLS). Specimens made by IM employed as raw material the commercial PA12 Evonik Vestamid, supplied in form of pellets, with the main manufacturing parameters detailed in Table 1. The SLS samples were processed in an EOS Formiga P-100 LS machine with a CO_2 laser, employing EOS

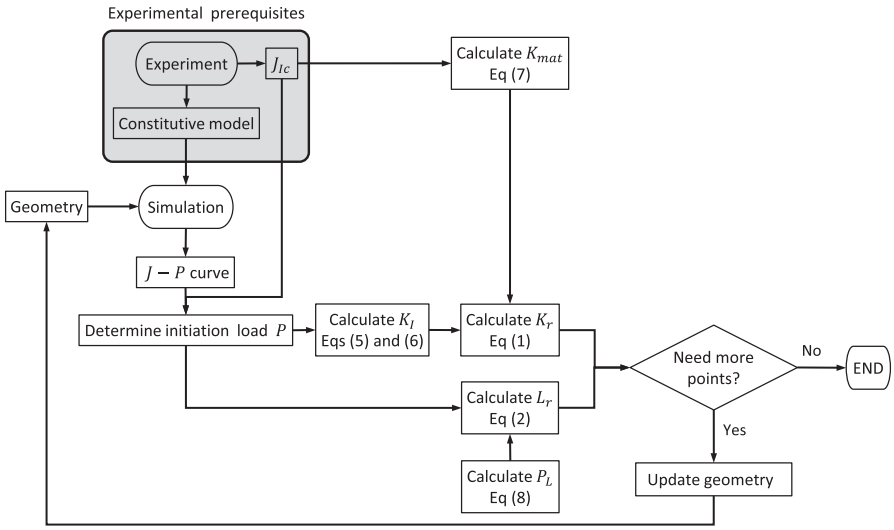

Fig. 2. Flowchart of the procedure to obtain the locus of the FAD.

PA2200 powder, and using the parameters described in Table 2.

Different specimen configurations were fabricated. In case of SLS, two batches of specimens with different orientation were manufactured for each configuration due to the layer-wise processing technique. In the batch named 0°, the layered structure was orientated parallel to the applied force while in the batch named 90°, the layers were perpendicular to the applied force (Fig. 1).

2.2. Mechanical characterization

The mechanical characterization consisted of tensile and fracture tests at room temperature performed following the guidelines given by ASTM D638 [17] and ASTM E1820 [18] standards, respectively. For the former, dumbbell samples were employed with nominal dimensions of the gage length of $6 \times 4 \times 33$ mm^3 and of $10 \times 4 \times 60$ mm^3 for the SLS and IM samples, respectively. For the latter, compact tension specimens were used with 40 mm in width and 10 mm in thickness. A natural crack was introduced via tapping a razor blade frozen at liquid nitrogen temperature placed on the root of a machined notch of 16 mm in length. The final initial crack length (machined notch plus natural crack), a_0, to width ratio was of 0.5. The notch sharpening method is an open issue that is still under investigation [19–20]. ESIS TC4 (European Structural Integrity Society Technical Committee 4 is currently working on this subject but at this moment, the fracture characterization protocols developed by ESIS TC4 have recognized the tapping procedure adequate for natural crack growth initiation in those materials where this method can be implemented [21].

The tests were carried out in a universal servohydraulic testing machine MTS 810 Material Testing equipped with a load cell of $\pm$ 5 kN and at a crosshead speed of 5 mm/min. For the tensile tests, ISO 527 [22] standard was followed. A contact extensometer (MTS 634.12F-24) was used to measure the longitudinal deformation, but also a 2-dimensional video correlation system was employed to obtain the 2-dimensional displacement field, in particular, the longitudinal and the transverse deformation. For the use of this technique, a previous preparation of the specimen surface was needed. Specifically, the surface was sprayed with black paint to attain a random, matte pattern of speckles that will be used as reference points to follow their movement during the test. Digital Image Correlation (DIC) allowed the determination of the current specimen dimensions and from them, the true stress and the true strain data without the volume constancy hypothesis even after necking occurrence. For the fracture characterization, a crack opening displacement transducer COD (MTS 632.02F-20) with a displacement range of + 3.9 mm/-2 mm was used for the crack growth determination using the compliance method [18].

3. FAD methodology

3.1. Numerical procedure

Fig. 2 shows the flowchart that describes the procedure to obtain the locus of the FAD. Prior to initiate the numerical simulation, experimental data is needed to feed the simulation. Mechanical characterization is carried out as explained in section 2.2 (obtention of the tensile properties).

As a thermoplastic, the mechanical behaviour of the PA12 evaluated in this work can be modelled through the hardening law developed by G'Sell et al. [12]:

$$\sigma = K^*\left(1 - e^{-\varepsilon/\varepsilon_v}\right)e^{h\varepsilon^2} \tag{4}$$

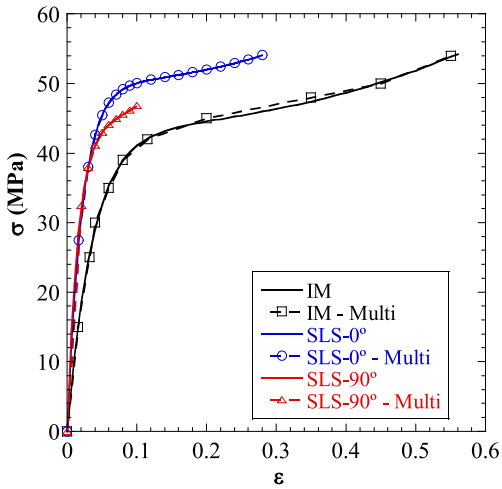

Fig. 3. True stress–strain curves comparing the multilinear model and G'Sell et al. [12] model for IM PA12 and SLS PA12 at 0° and 90° orientations.

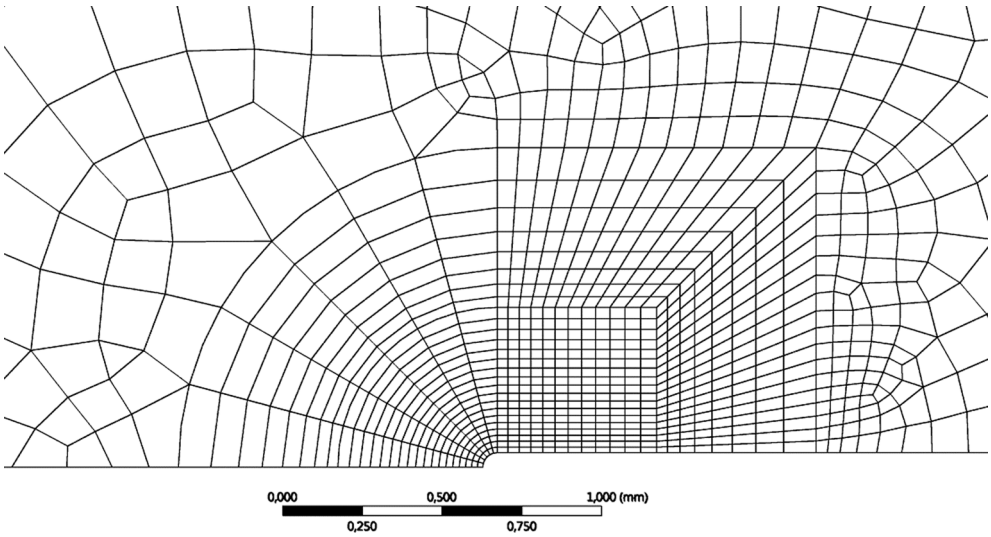

Fig. 4. Mesh at the crack tip.

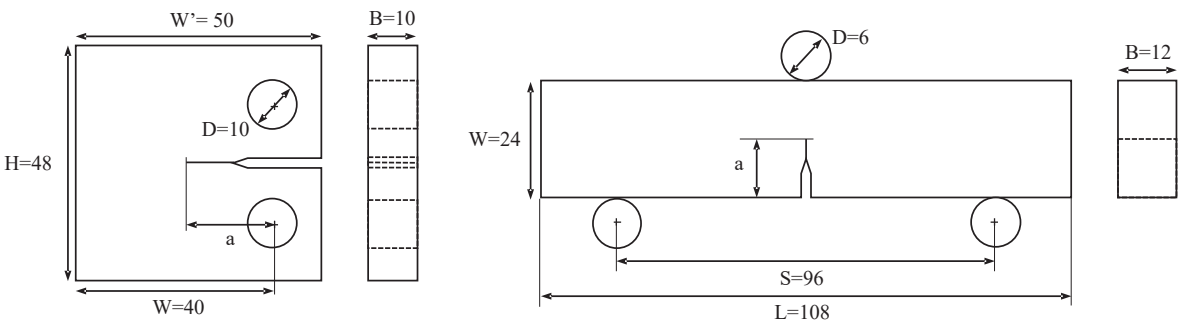

Fig. 5. Specimens' dimensions schemes. Lengths in millimetres.

Where K^* is a material constant related to the yield strength including the strain rate term ($K^* = K\dot{\varepsilon}^m$, as compared with Eq. (3)). This behaviour was introduced in the Finite Element Analysis (FEA) through the Multilinear Isotropic Hardening model available in predefined ANSYS Mechanical models assuming a uniform strain rate and fitting the model with the PA12 properties (Fig. 3). This is a

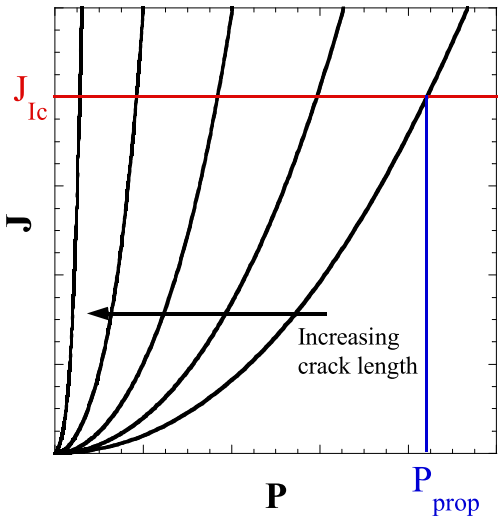

Fig. 6. $J-P$ driving force diagrams.

first approximation due to the strain rate gradient at the crack tip front. The tensile and fracture experiments were carried out at the same crosshead rate to have relatively comparable scenarios.

Once the model is defined (tensile properties) and a desired configuration (geometry) is settled, the FEA is to be performed. In this work, a 3D geometry discretized with quadratic hexahedrons is used. Only one fourth of the model has been simulated taking advantage of the symmetry of the problem in all configurations (see Fig. 4). In order to ease J-integral calculations, a contoured mesh at the crack tip has been meshed. The chosen contour to make the computations was distant enough from the crack tip to avoid any influence of the elements' distortion.

Two geometrical configurations have been employed in the numerical simulations: Compact Tension (CT) and Single Edge Notched Bending (SENB) specimens. A scheme of these specimens with their dimensions is shown in Fig. 5. The following crack lengths were chosen as 15, 20, 25, 30 and 35 mm for the CT specimens and 12, 14, 16, 18, 20 and 22 mm for the SENB specimens, being S the span length in this case.

Following the flowchart in Fig. 2, from the J-integral simulations, J, and load, P, values are recorded and $J-P$ curves are constructed. Knowing the critical value of J-integral, J_{Ic}, (prior fracture characterisation as described in section 2.2) one can predict the value of the load at which the crack would start propagation, P_{prop} (see Fig. 6).

At this extent, the stress intensity factor, K_I, can be computed for the predicted load of crack propagation, P_{prop}, from Eq. (5).

$$K_I = \frac{P_{prop}}{B\sqrt{W}} f\left(\frac{a}{W}\right) \tag{5}$$

Where $f(a/W)$ is a geometric factor dependent on the crack length to width ratio, a/W, and configuration. The tabulated expressions of $f(a/W)$ for the analysed specimens [7] are given by:

$$\begin{aligned} f\left(\frac{a}{W}\right) &= \frac{2+\frac{a}{W}}{\left(1-\frac{a}{W}\right)^{\frac{3}{2}}}\left[0.886+4.64\left(\frac{a}{W}\right)-13.32\left(\frac{a}{W}\right)^2+14.72\left(\frac{a}{W}\right)^3-5.6\left(\frac{a}{W}\right)^4\right] \& forCT \\ f\left(\frac{a}{W}\right) &= \frac{3\frac{S}{W}\sqrt{\frac{a}{W}}}{2\left(1+2\frac{a}{W}\right)\left(1-\frac{a}{W}\right)^{\frac{3}{2}}}\left\{1.99-\frac{a}{W}\left(1-\frac{a}{W}\right)\left[2.15-3.93\left(\frac{a}{W}\right)+2.7\left(\frac{a}{W}\right)^2\right]\right\} \& forSENB \end{aligned} \tag{6}$$

Therefore, K_r is directly obtained by Eq. (1) and K_{mat} is defined by:

$$K_{mat} = \sqrt{J_{Ic}E} \tag{7}$$

where K_{mat} is the fracture toughness in plane stress condition in terms of J-integral and E the elastic modulus. On the other hand, the collapse load, P_L, is to be computed from Eq. (8) [7] in also plane stress conditions through:

Table 3
Young's modulus, E, the Poisson's ratio, ν, the yield strength, σ_y, the tensile strength, σ_U, and the elongation at break, ε_R, the parameters of the G'Sell et al. [12] stress–strain equation Eq. (3) and J-integral at crack growth initiation, J_{Ic}, of PA12 manufactured by IM and by SLS at 0° and 90° orientations [23].

		Tensile properties								Fracture properties
		E(MPa)	ν	σ_y(MPa)	σ_U(MPa)	ε_R(%)	Stress–strain equation parameters			
							K^*(MPa)	ε_v(%)	h	J_{Ic}(kJ/m^2)
IM		1.29 ± 0.04	0.46 ± 0.02	41 ± 1	54 ± 1	64 ± 3	43	3.60	0.7	8.1 ± 1.2
SLS	**0°**	1.64 ± 0.03	0.43 ± 0.02	47 ± 1	53 ± 2	27 ± 2	50	2.10	1.0	7.0 ± 0.6
	90°	1.58 ± 0.04	0.41 ± 0.01	44 ± 2	46 ± 5	10 ± 4	44	1.54	6.4	6.7 ± 1.2

$$\begin{aligned} P_L &= 1.072\eta B(W-a)\left(\frac{\sigma_y+\sigma_U}{2}\right) \\ \eta &= \sqrt{\left(\frac{2a}{W-a}\right)^2+\frac{4a}{W-a}+2}-\left(\frac{2a}{W-a}+1\right) \quad \&forCT \\ P_L &= \frac{1.072B(W-a)^2}{S}\left(\frac{\sigma_y+\sigma_U}{2}\right)\&forSENB \end{aligned} \tag{8}$$

Where σ_y is the yield strength and σ_U is the tensile strength. Hence, L_r is obtained for the load at the crack growth initiation, P_{prop}, from Eq. (2). Finally, K_r and L_r are found for a geometry. These steps must be repeated for each desired geometric configuration until enough points of the $K_r - L_r$ diagram (FAD) are attained.

3.2. BS 7910 standard

The British Standard BS 7910 [8] proposes two options to obtain the FAD for metallic materials that do not imply the necessity of dealing with Finite Element Analysis of the evaluated component. The first option (Option 1) just depends on few material properties: E, σ_y, σ_U. The FAD can be calculated as a function of these material properties and L_r as shown in Eq. (9) .

$$\left.\begin{aligned} f(L_r) &= \left(1+\frac{1}{2}L_r^2\right)^{-\frac{1}{2}}\left[0.3+0.7e^{-\mu L_r^6}\right]\&L_r \le 1 \\ f(L_r) &= f(1)L_r^{\frac{N-1}{2N}}\&1 < L_r < L_{r,max} \\ f(L_r) &= 0\&L_r \ge L_{r,max} \end{aligned}\right\} \tag{9}$$

Being the constants μ and N defined as Eq. (10).

$$\begin{aligned} \mu &= \min\left(0.001\frac{E}{\sigma_y};0.6\right) \\ N &= 0,3\left(1-\frac{\sigma_y}{\sigma_U}\right) \end{aligned} \tag{10}$$

Option 1 settles a conservative scenario in the evaluation of the metallic component's integrity. A less conservative choice is Option 2 which is computed from the expression in Eq. (11).

$$\left.\begin{aligned} f(L_r) &= \left(\frac{E\varepsilon_{ref}}{L_r\sigma_y}+\frac{L_r^3\sigma_y}{2E\varepsilon_{ref}}\right)^{-1/2}\&L_r < L_{r,max} \\ f(L_r) &= 0\&L_r \ge L_{r,max} \end{aligned}\right\} \tag{11}$$

Where ε_{ref} is the reference strain at a given reference stress, σ_{ref}, which can be defined as $\sigma_{ref} = L_r\sigma_y$.

The elastic modulus corresponds to the slope or derivative of the linear-elastic region of stress–strain curve. For some polymers, this linear relationship is doubtful, as the G'Sell et al. [12] model demonstrates in Eq. (4). So, to overcome this difficulty, an alternative was chosen that consisted in replacing the elastic modulus in Eq. (11) with the slope of the stress–strain curve shown in Eq. (12).

$$\frac{d\sigma}{d\varepsilon} = 2hK^*\varepsilon e^{h\varepsilon^2}\left(1-e^{-\varepsilon/\varepsilon_v}\right)+\frac{K^*e^{h\varepsilon^2-\varepsilon/\varepsilon_v}}{\varepsilon_v} \tag{12}$$

Once again, the underlying hypothesis of uniform strain rate is assumed.

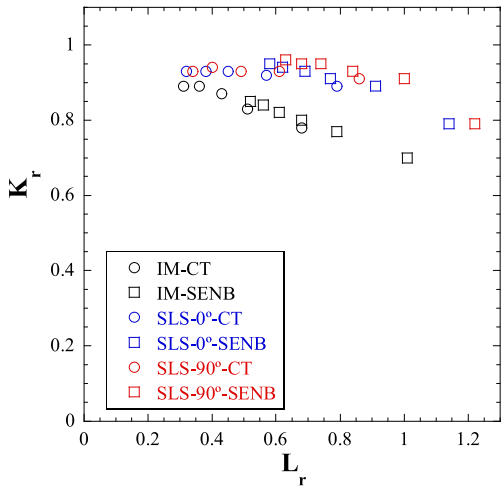

Fig. 7. Failure Assessment Line obtained for IM PA12 and SLS PA12 at 0° and 90° orientations.

Table 4
Collapse load, P_L, loading ratio, L_r, and stress intensity factor ratio, K_r, values for IM PA12 and SLS PA12 at 0° and 90° orientations for each geometric configuration.

Specimen	Crack Length (mm)	Collapse load, P_L (N)			L_r			K_r		
		IM	SLS-0°	SLS-90°	IM	SLS-0°	SLS-90°	IM	SLS-0°	SLS-90°
CT	15	2757	2903	2612	0.31	0.32	0.34	0.89	0.93	0.93
	20	1653	1740	1566	0.36	0.38	0.40	0.89	0.93	0.94
	25	870	916	824	0.43	0.45	0.49	0.87	0.93	0.93
	30	362	381	343	0.51	0.57	0.61	0.83	0.92	0.93
	35	85	89	80	0.68	0.79	0.86	0.78	0.89	0.91
SENB	12	917	965	868	0.52	0.58	0.63	0.85	0.95	0.96
	14	637	670	603	0.56	0.62	0.68	0.84	0.94	0.95
	16	407	429	386	0.61	0.69	0.74	0.82	0.93	0.95
	18	229	241	217	0.68	0.77	0.84	0.80	0.91	0.93
	20	102	107	96	0.79	0.91	1.00	0.77	0.89	0.91
	22	25	27	24	1.01	1.14	1.22	0.70	0.79	0.79

4. Results

4.1. Mechanical properties

In Fig. 3. shows the representative true stress – strain curves of PA12 manufactured via IM and SLS at 0° and 90° orientations. The parameters of the model in Eq. (4) are collected in Table 3, together with the Young's modulus, E, the Poisson's ratio, ν, the yield strength, σ_y, the tensile strength, σ_U and the elongation at break, ε_R, obtained from the tensile tests, and the J-integral at crack growth initiation, J_{Ic}, obtained from the fracture tests [23].

First of all, the results obtained in the tensile tests agree with the literature in both groups of samples, IM [24] and SLS [1]. The main unquestionable difference between the specimens manufactured by IM and by SLS is the elongation at break, being in the injected specimens more than double that of those manufactured by additive techniques. In addition, the elastic modulus and yield strength were lower in the IM specimens, 25% and 12%, respectively. The only mechanical magnitude measured experimentally where the injected specimens presented higher values was the J-Integral at crack growth initiation, reaching IM values 20% higher than those of SLS. When comparing the SLS specimens in the two orientations tested, once again the elongation at break was the main difference, the rest of the magnitudes being really very similar.

4.2. Failure Assessment diagrams (FAD)

Fig. 7 displays the FAD obtained for the three materials under study, IM PA12 and SLS PA12 at 0° and 90° orientations. The L_r and K_r values together with the collapse load, P_L, for each material and geometric configuration are gathered in Table 4. Significant differences are found between IM and SLS specimens. While SLS PA12 is very consistent with the Linear Elastic Fracture Mechanics (LEFM) approach in most of the L_r range since K_r values are almost constant and close to 0.95, IM PA12 is under larger effect of

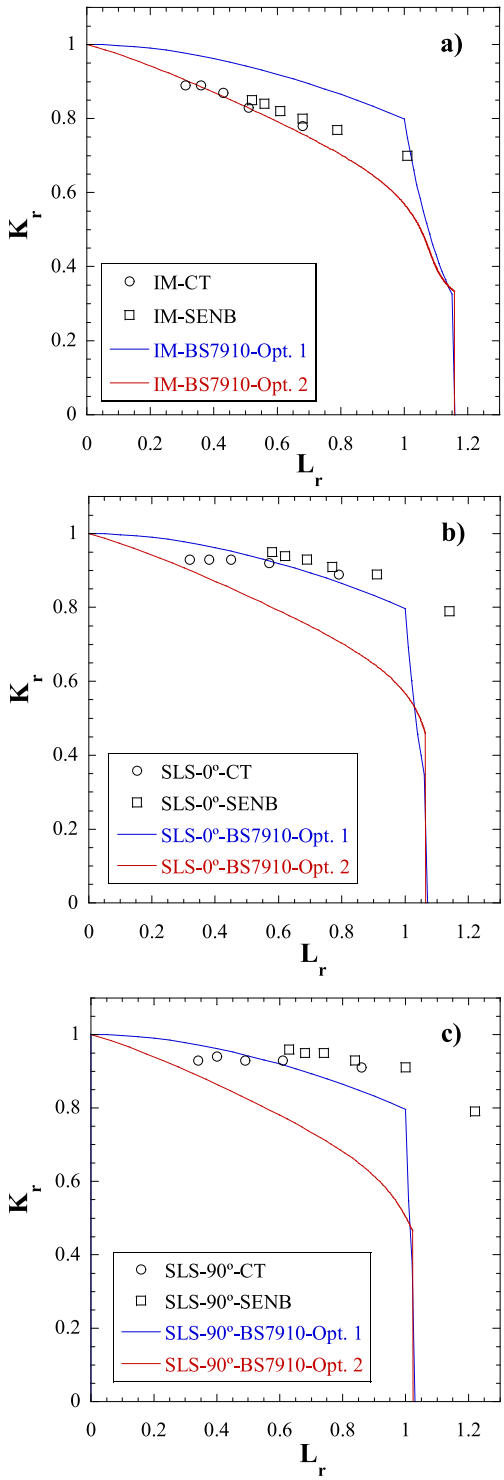

Fig. 8. Failure Assessment Lines from Options 1 and 2 of BS 7910 and points obtained by FEA for a) IM PA12 and SLS PA12 at b) 0° and at c) 90° orientations.

plasticity, showing a more pronounced decrease in K_r values when increasing L_r. Regarding the different orientations in SLS PA12, the FAD of SLS PA12 at 90° orientation is slightly above that of SLS PA12 at 0° orientation.

These diagrams reflect the mechanical behavior of each material accurately. Beginning with the effect of the manufacturing process, the main difference between IM PA12 and SLS PA12 is ductility. The larger values of the elongation at break presented by IM

PA12, as well as its higher energy at crack growth initiation (Table 3), indicates that the fracture in IM samples is prone to occur in combination with plasticity effects as the applied stress increases. This leads to a monotonous decrease in K_r values as the load ratio L_r rises (Fig. 7). On the other hand, SLS PA12 is rather brittle, especially, at 90° orientation, partly due to the weak interface strength between layers. The detriment of plasticity during fracture implies small deviation from linearity and accounts for almost horizontal FAD. Besides, the lower ductility of SLS PA12 at 90° orientation also justifies that its fracture line is located slightly above that of the 0° orientation.

Fig. 8 shows the FAD previously shown in Fig. 7 together with the options 1 and 2 proposed by the BS 7910. In general, none of the options proposed by the BS 7910 standard adequately fits the numerical results obtained in this work. Nevertheless, some considerations can be made in this regard. From the IM samples, it's evident that option 1 is more of an insecure locus than a conservative one. Not only the failure points obtained through FEA are within the integrity region of option 1, but option 2 is also contained within the locus of option 1. In fact, this problem is also present for the SLS samples, indicating the link between option 1 and Ramberg-Osgood behavior and its inconvenience when evaluating the structural integrity of thermoplastic components. Modified Option 2, Eqs. (11) and (12), has shown a better fit to the results. It has been proven to be adequate for low values of Lr and conservative for high values of Lr. [12].

BS7910 option 1 and option 2 predictions are not good for SLS samples. Nothing different could be expected given the limited ductility of the materials thus manufactured. The linear elastic fracture mechanics (LEFM) approach is the best alternative in practically the entire range of L_r values. Plasticity effects are mostly negligible.

5. Conclusions

This work has determined the Failure Assessment Diagrams of PA12 manufactured via injection moulding and Selective Laser Sintering. The diagrams were obtained via numerical J-integral calculus using the G'Sell et al. material model to approximate the behaviour of PA12. The diagrams obtained were compared to those calculated using the options of the BS 7910 standard. This investigation revealed that none of the BS 7910 options showed good fit with the FEA results.

IM PA12 showed a clear decrease in K_r values when increasing L_r. This contrasted with SLS PA12 diagrams, in which K_r values maintained almost constant and close to 0.95 independently of L_r. Regarding the orientation in SLS PA12, the diagram attained at 90° orientation was slightly above that computed at 0° orientation, indicating the more brittle behavior of the former due to the weak adhesion strength among layers.

CRediT authorship contribution statement

M. Martínez: Conceptualization, Methodology, Investigation. Writing – Original Draft. **A. J. Cano:** Methodology, Investigation. **A. Salazar:** Conceptualization, Methodology, Investigation, Writing – Review & Editing. **J. Rodríguez:** Conceptualization, Methodology, Writing – Review & Editing, Funding acquisition.

Declaration of Competing Interest

The authors declare that they have no known competing financial interests or personal relationships that could have appeared to influence the work reported in this paper.

Acknowledgement

Authors are indebted to Ministerio de Economía y Competitividad of Spain for their financial support through grant DPI2016-80389-C2-1-R and to Ministerio de Ciencia, Innovación y Universidades through grant PID2019-108968RB-I00. The authors also wish to thank Dr. Javier Gomez of Advanced Materials Simulation for his fruitful discussions.

References

[1] Dupin S, Lame O, Barrès C, Charmeau J. Microstructural origin of physical and mechanical properties of polyamide 12 processed by laser sintering. Eur Polym 2012;48:1611–21.
[2] Goodridge R, Ziegelmeier S. 7 - Powder bed fusion of polymers. In: Brandt M, editor. Laser Additive Manufacturing. Woodhead Publishing; 2017. p. 181–204.
[3] Anonymous Additive Manufacturing Opportunities In Automotive. S. Publishing (2018).
[4] Anonymous Wohlers Report. Wohlers Associates (2019).
[5] Dizon JRC, Espera AH, Chen Q, Advincula RC. Mechanical characterization of 3D-printed polymers. Addit Manuf 2018;20:44–67.
[6] Deshmukh K, Muzaffar A, Kovářík T, Křenek T, Ahamed MB, Pasha SKK. Chapter 17 - Fundamentals and applications of 3D and 4D printing of polymers: Challenges in polymer processing and prospects of future research. In: Sadasivuni KK, Deshmukh K, Almaadeed MA, editors. 3D and 4D Printing of Polymer Nanocomposite Materials. Elsevier; 2020. p. 527–60.
[7] Anderson TL. FRACTURE MECHANICS: Fundamentals and Applications, Fourth. edition ed. Boca Raton, FL: CRC Press; 2017.
[8] Bsi. Guide to methods for assessing the acceptability of flaws in metallic structures. BS 2013;7910:2013.
[9] API, ASME, Fitness-For-Service. API 579-1/ASME FFS-1 (2016).
[10] G'sell C, Jonas JJ. Determination of the plastic behaviour of solid polymers at constant true strain rate. J Mater Sci 1979;14:583–91.
[11] G'Sell C, Jonas JJ. Yield and Transient Effects During the Plastic Deformation of Solid Polymers. J Mater Sci 1981;16:1956–74.
[12] G'sell C, Aly-Helal NA, Jonas JJ. Effect of stress triaxiality on neck propagation during the tensile stretching of solid polymers. J Mater Sci 1983;18:1731–42.
[13] Meijer HEH, Govaert LE. Mechanical performance of polymer systems: The relation between structure and properties. Prog Polym Sci 2005;30:915–38.

[14] Cicero S, Madrazo V, Carrascal IA, Cicero R. Assessment of notched structural components using Failure Assessment Diagrams and the Theory of Critical Distances. Eng Fract Mech 2011;78:2809–25.
[15] Ibáñez-Gutiérrez FT, Cicero S. Fracture assessment of notched short glass fibre reinforced polyamide 6: An approach from failure assessment diagrams and the theory of critical distances. Compos B Engng 2017;111:124–33.
[16] Fuentes JD, Cicero S, Ibáñez-Gutiérrez FT, Procopio I. On the use of British standard 7910 option 1 failure assessment diagram to non-metallic materials. Fatigue Fract Eng Mater Struct 2018;41:146–58.
[17] ASTM, Standard Test Method for Tensile Properties of Plastics. ASTM D638-14 (2015).
[18] ASTM, Standard Test Method for Measurement of Fracture Toughness. ASTM E1820-18ae1 (2018).
[19] Salazar A, Rodríguez J, Segovia A, Martínez AB. Relevance of the femtolaser notch sharpening to the fracture of ethylene–propylene block copolymers. Eur Polym J 2010;46(9):1896–907.
[20] Martínez AB, León N, Arencón D, Rodríguez J, Salazar A. On the effect of the different notching techniques on the fracture toughness of PETG. Polym Test 2013; 32(7):1244–52.
[21] Moore DR, Pavan A, Williams JG. Fracture mechanics testing methods for polymers, adhesives and composites. Elsevier; 2001.
[22] ISO, Plastics — Determination of tensile properties — Part 1: General principles. ISO 527-1:2019 (2019).
[23] Cano AJ, Salazar A, Rodríguez J. Effect of temperature on the fracture behavior of polyamide 12 and glass-filled polyamide 12 processed by selective laser sintering. Eng Fract Mech 2018;203:66–80.
[24] Van Hooreweder B, Moens D, Boonen R, Kruth J, Sas P. On the difference in material structure and fatigue properties of nylon specimens produced by injection molding and selective laser sintering. Polym Test 2013;32:972–81.